Impact of Failure on the Tilt-Wing eVTOL Backward Transition

Marc May and Daniel Milz and Sophie F. Armanini and Gertjan Looye

The backward transition from cruise to hover flight is the crucial flight maneuver for tilt-wing aircraft, as it allows for a safe vertical landing. Unfortunately, this flight phase is especially challenging due to low thrust settings and thereby reduced slipstream effects, which push the wing states toward or beyond flow separation. This raises the question of how failure conditions further impact these already severe conditions, and if the remaining flight performance suffices to perform the backward transition. This study therefore assesses the tilt-wing's fault tolerance against single and combined component failures. The reference scenario of a longitudinal level backward transition is investigated with optimal-control-based trajectory optimization on a 6DoF aircraft model. The results indicate fault tolerance of the tilt-wing aircraft for most failure cases. The majority of failure cases leading to unfeasible transition trajectories suffer from unbalanced hover or cruise conditions. Only for the failure case of control surface runaways on the same side of canard and main wing, the transition maneuver itself is the limiting factor due to increased thrust settings and thus longer transition times.

Impact of Failure on the Tilt-Wing eVTOL Backward Transition

Marc May* and Daniel Milz†
Institute of System Dynamics and Control, German Aerospace Center (DLR), 82234 Weßling, Germany
eAviation Lab, TUM School of Engineering and Design, 85521 Ottobrunn, Germany

Sophie F. Armanini ‡
Aerial Robotics Laboratory, Imperial College London, London SW7 2AZ, UK

Gertjan Looye§
Institute of System Dynamics and Control, German Aerospace Center (DLR), 82234 Weßling, Germany

The backward transition from cruise to hover flight is the crucial flight maneuver for tilt-wing aircraft, as it allows for a safe vertical landing. Unfortunately, this flight phase is especially challenging due to low thrust settings and thereby reduced slipstream effects, which push the wing states toward or beyond flow separation. This raises the question of how failure conditions further impact these already severe conditions, and if the remaining flight performance suffices to perform the backward transition. This study therefore assesses the tilt-wing's fault tolerance against single and combined component failures. The reference scenario of a longitudinal level backward transition is investigated with optimal-control-based trajectory optimization on a 6DoF aircraft model. The results indicate fault tolerance of the tilt-wing aircraft for most failure cases. The majority of failure cases leading to unfeasible transition trajectories suffer from unbalanced hover or cruise conditions. Only for the failure case of control surface runaways on the same side of canard and main wing, the transition maneuver itself is the limiting factor due to increased thrust settings and thus longer transition times.

I. Introduction

Tiltwing aircraft promise to combine the advantages of efficient lift-borne cruise flight and vertical take-off and landing (VTOL) capability. These characteristics allow to establish efficient, flexible, and time-saving transport options without high demands on ground infrastructure. The key flight phase for tilt-wing aircraft is the backward transition maneuver, as it is mandatory to allow for a safe vertical landing and thus to complete the flight mission at the intended destination. At the same time, this maneuver is highlighted in [1, 2] as the most challenging and complex one. The difficult conditions arise chiefly from high angles of attack (AoA) with flight close to or even beyond flow separation, and low thrust settings which lead to diminished positive slipstream effects. The backward transition gets even more challenging when considering failure scenarios and raises the question of how the vehicle can still land safely under these conditions. However, eVTOLs in general are equipped with a large number of actuators and engines, thus providing high levels of redundancy. Still, certain failure combinations might significantly impact the remaining flight performance. With that in mind, this paper analyses the impact of failure conditions on the backward transition maneuver in order to identify and analyze failure combinations that impede the conventional backward transition and consequently also the vertical landing.

A. State of the Art

Preparing the analysis of transition flight under failure conditions, the literature research first shows the approaches for nominal dynamic transition trajectory optimization before giving an overview of eVTOL safety aspects.

Transition Analysis Optimal control (OC) is a common approach to find state trajectories of nonlinear and even unstable dynamic systems without having to design a stabilizing feedback controller. The resulting trajectories exploit

*Research Assistant, marc.may@dlr.de, AIAA member
†Research Assistant, daniel.milz@dlr.de, AIAA member
‡Senior Lecturer, Aerial Robotics Laboratory, Imperial College London
§Head of Department, gertjan.looye@dlr.de, AIAA member

(almost) full plant capabilities, as the method provides optimal control policies depending on the formulation of objective and constraint. It thus allows to either dynamically analyze unfamiliar systems, or to improve the performance of feedback controllers by providing feedforward terms. In [3–6], the OC approach is applied for the investigation of tilt-wing transition flight. Panish and Bacic [6] investigate the remaining transition performance for various weight and balance settings, which is similar to investigating abnormal or failure conditions. However, [6] only considers purely longitudinal motion in flight path coordinates with 3 degrees of freedom (DoF), similar to our former work on different transition strategies [2]. In contrast, Lu et al. [7] deploy our linear tilt-wing model from [8] to find 6DoF multi-phase trajectories.

The transition maneuver has also been studied for other, similar eVTOL configurations. From a flight mechanic perspective, especially tailsitter transition flight results in comparable behavior. Instead of tilting the wing relative to the fuselage, the tailsitter changes its pitch attitude during the transition maneuver. That way, rotors and wings likewise stay aligned, which results in similar effective angles of attack and aero-propulsive interactions as encountered during tilt-wing transition. While [9] uses a general formulation for the transition, Kubo and Suzuki [11] optimize for different transition strategies and verify them experimentally. Introducing a constraint to avoid flow separation, [10] exploits vertical motion to maintain low effective AoA. The same strategy can be applied for tilt-wing aircraft [2, 12]. Engine failures are considered for eVTOLs in [13, 14], where the remaining maneuverability (in form of the attainable maneuverability zone) is estimated with OC.

Safety Aspects Safety is a crucial factor for the success of a technology. This especially counts for aviation, where accidents often have catastrophic extent, obviously for directly involved people like passengers and crew, but also for third parties. History shows that reputation in aviation is quickly lost if safety is not guaranteed. This was experienced in the *helicopter era* in the 60s and 70s, where VTOL operations in several American cities ceased - next to other reasons - after fatal accidents [15]. Today, safety is highlighted as the most important factor for the adoption of Air Mobility (AM) by a majority of people [16, 17]. At the same time, new, complex, and unfamiliar systems like eVTOLs increase the likelihood of failure events [18]. Thus, it seems reasonable to consider the impact of failures on the remaining flight performance to allow for establishing countermeasures in vehicle design, vehicle operation, and air traffic management.

While for a complex system like an eVTOL, there is a long list of potential hazards for aircaft safety, most work in literature is focused on propulsion failure [13, 14, 18–20]. The research is often aligned with the single failure criteria of the SC-VTOL [21]. On the actuation side, there are also control surfaces and the wing tilt actuation that can fail. Other causes for a reduced flight performance could be external disturbances like (extreme) winds [19], structural damage (e.g. due to bird strike or mid-air collision) [18], or a change in weight and balance (WaB) [6].

B. Scope of this Paper

This paper investigates the impact of single and combined failures on the remaining tilt-wing flight performance during the backward transition. While there are numerous potential causes for diminished flight performance, this work is limited to rotor and control surface failures. To obtain the largest impact on flight performance, rotor failures are modeled as full losses and control surface failures as runaways to the deflection limits. These failures will introduce asymmetry to the aircraft behavior, wherefore a 6DoF model is required, although the aircraft motion during transition is limited to be purely longitudinal. To properly capture the aircraft aerodynamic characteristics, a compromise of the full strip theory model [22] and its 2D-representation [2] is achieved in form of a *minimum strip* model. For the analysis, the optimal control framework from [2] and conventional trim investigations are deployed. First, the nominal transition trajectory is analyzed to give a reference, before all failure combinations are tested. While a successful trajectory optimization suggests that the aircraft is still capable of flying the backward transition, an unsuccessful optimization does not necessarily imply that the transition is no longer possible. Therefore, a detailed assessment of those failure cases has to follow.

II. 6DoF Trajectory Optimization

The failure analysis is conducted on the tandem tilt-wing configuration shown in Fig. 1(a). Both wings can be deflected by tilt angle in the range $\delta_w \in [0°, 90°]$, where zero deflection corresponds to cruise flight with an alignment of wing chord and the body x-axis x^B (see Fig. 1(a)), and $\delta_w = 90°$ corresponds to hovering flight with the propellers facing upward. Each wing is equipped with four propellers and two control surfaces respectively. The direction of rotation for the total eight propellers is given in Fig. 1(a), whereas the control surface deflections $\delta_e \in [-30°, 30°]$ are defined to be positive for a local increase of airfoil lift (mathematically positive direction of rotation around y^B). For the failure analysis, the optimal control framework presented in [2] has to be extended. However, the convergence and computation time of the optimal control approach highly depends on the model complexity. Consequently, a compromise with regard to fidelity is required. Our former transition analysis was limited to longitudinal aircraft motion, thereby significantly reducing the problem size. This was justified by the aircraft symmetry with respect to the x-z-plane under nominal conditions. However, introducing failure conditions, the symmetry assumption no longer holds, and a full 6DoF model has to be applied. To cover slipstream effects for asymmetric propeller settings and surface deflections along a wing, the 2D aerodynamic model is no longer sufficient and likewise needs to be extended. As a compromise between the former modeling approaches of 2D [2] and full strip theory [22] aerodynamic models, we develop a strip-based model using the minimum number of strips to capture the averaged upwash and downwash of each propeller half-plane. This results in a number of 12 strips for the wings - because the outer propeller half-plane protrudes beyond the wing span - and 4 strips for the lateral stabilizers. In the following, the model will be called *minimum strip* (or in short "3D") model. All model components are illustrated in Fig. 1, and the indices are assigned according to Table 1.

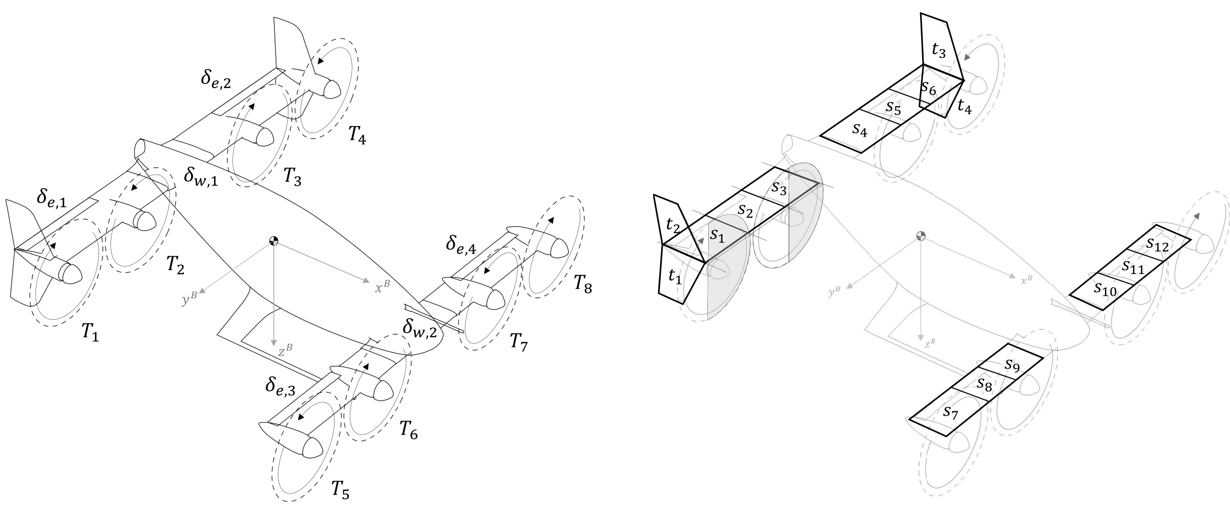

(a) (b)

Fig. 1 3D view of the tandem tilt-wing configuration (a), and illustration of the minimum strip aerodynamic model (b).

Component	Index	Range
Wing	i	1..2
Control Surface	k	1..4
Propeller	p	1..8
Wing Strip	s	1..12
Wing Tip Strip	t	1..4

Table 1 Component indices of Fig. 1.

A. 6 DoF Tilt-Wing Model

The equations of motion (EoM) for 6DoF flight relative to a non-rotating flat earth inertial frame $\mathcal{F}_E$ are:

$$\dot{\boldsymbol{v}}^B = \frac{\sum \boldsymbol{f}^B}{m} - \boldsymbol{\omega}^B \times \boldsymbol{v}^B \tag{1}$$

$$\dot{\boldsymbol{\omega}}^B = I^{-1}\left(\sum \boldsymbol{m}^B - \boldsymbol{\omega}^B \times I\boldsymbol{\omega}^B\right) \tag{2}$$

with force vector $\boldsymbol{f}^B$, moment vector $\boldsymbol{m}^B$, and translational $\boldsymbol{v}^B$ and rotational ω^B velocities, all defined in the body frame $\mathcal{F}_B$. I and m represent inertia and mass. The resulting force and moment vectors are obtained by summation over the individual contribution of the 8 propellers (subscript P), 12 wing strips (subscript A) and 4 wing tip strips (subscript S). In addition, the effect of airfoils mounted to the landing skids (called *inverted V*, subscript V) is included. The fuselage drag (subscript F) and gravity (subscript G) are assumed to act directly at the center of gravity (CG) and thus have no moment contribution.

$$\boldsymbol{f}^B = \sum_{p=1}^{8} \boldsymbol{f}^B_{P,p} + \sum_{s=1}^{12} \boldsymbol{f}^B_{A,s} + \sum_{t=1}^{4} \boldsymbol{f}^B_{S,t} + \boldsymbol{f}^B_V + \boldsymbol{f}^B_F + \boldsymbol{f}^B_G \tag{3}$$

$$\boldsymbol{m}^B = \sum_{p=1}^{8} \boldsymbol{m}^B_{P,p} + \sum_{s=1}^{12} \boldsymbol{m}^B_{A,s} + \sum_{t=1}^{4} \boldsymbol{m}^B_{S,t} + \boldsymbol{m}^B_V \tag{4}$$

For the computation of the resulting moment due to applied forces, the lever arm $\boldsymbol{r}$ from each component's reference point to the CG has to be considered:

$$\boldsymbol{m}^B_{P,p} = \boldsymbol{r}_p \times \boldsymbol{f}^B_{P,p} + \boldsymbol{R}_{\mathrm{wb,i}} \begin{bmatrix} Q_p & 0 & 0 \end{bmatrix}^T \tag{5}$$

$$\boldsymbol{m}^B_{A,s} = \boldsymbol{r}_s \times \boldsymbol{f}^B_{A,s} + \begin{bmatrix} 0 & M_{y,s} & 0 \end{bmatrix}^T \tag{6}$$

$$\boldsymbol{m}^B_{S,t} = \boldsymbol{r}_t \times \boldsymbol{f}^B_{S,t} \tag{7}$$

$$\boldsymbol{m}^B_V = \boldsymbol{r}_V \times \boldsymbol{f}^B_V \tag{8}$$

$$\tag{9}$$

The rotation matrices from wing to body frame $\boldsymbol{R}_{\mathrm{wb,i}}$ is a function of the local wing tilt angle $\delta_{w,i}$ and used to rotate the propeller torque Q into the body frame. For a wing tilting purely around the y-axis, the airfoil pitching moment $M_{y,s}$ is equal in body and wing frame, and consequently does not need to be transformed. Usually, the rotor working state is defined by rotational speed Ω. Assuming constant rotor coefficients (the vehicle is equipped with variable blade pitch that adapts to the current propeller working state), the thrust equally defines the working state and there is a linear relationship between torque Q and thrust T:

$$Q_p = \pm T_p \frac{c_T}{c_Q} \frac{1}{D_P} \tag{10}$$

with thrust and torque coefficient c_T and c_Q, and propeller diameter D_P. The sign of the rotor torque depends on the direction of rotation according to Fig. 1(a). The rotor forces in body frame are

$$\boldsymbol{f}^B_{P,p} = \boldsymbol{R}_{\mathrm{wb,i}} \begin{bmatrix} T_p & 0 & 0 \end{bmatrix}^T \tag{11}$$

Without symmetry, the propeller induced swirl component has to be included in the computation of local strip velocities. To capture the effect of blade upwash and downwash, one strip per propeller half-plane is required, as illustrated in Fig. 1(b). The induced slipstream velocities of rotor p are

$$v_{\mathrm{iax},p} = -\frac{v^W_{x,p}}{2} + \sqrt{\left(\frac{v^W_{x,p}}{2}\right)^2 + \frac{T_p}{2\rho A_P}} \tag{12}$$

$$v_{\mathrm{it},p} = c_{\mathrm{vit}}\sqrt{T_p} \tag{13}$$

with air density ρ and rotor disk area $A_P = \pi D_P^2/4$. For the computation of propeller inflow $\boldsymbol{v}_p^W$, the effect of body rotation is neglected:

$$\boldsymbol{v}_p^W = \boldsymbol{R}_{\mathrm{wb,i}} \cdot \boldsymbol{v}^B \tag{14}$$

The constant c_{vit} in Eq. (13) averages the spanwise tangential velocity distribution over the width of a strip, and its derivation is given in the Appendix A.A. Note that Eq. (12) is the formulation for the axially induced speed in the propeller plane. Due to slipstream contraction, this velocity would accelerate up to $2 \cdot v_{\mathrm{iax}}$ for a fully contracted slipstream (according to momentum theory). However, the contracted slipstream does not wet the full strip area. When averaging over a strip, the effects of slipstream acceleration and unwetted area balance each other, and the velocity in the the propeller plane can be deployed.

In the following, only the computation of wing strip aerodynamics ($\boldsymbol{f}_{A,s}^B$,$\boldsymbol{m}_{A,s}^B$) is presented, as the computation is the same for the wing tip stabilizers and the *inverted V*. However, the latter is only approximated by a single vertical airfoil. The resulting total velocity at the aerodynamic center of each strip, located in the $c/4$-line, is:

$$\boldsymbol{v}_s^W = \boldsymbol{R}_{\mathrm{wb,i}} \cdot \left(\boldsymbol{v}^B + \boldsymbol{\omega}^B \times \boldsymbol{r}_s\right) + v_{\mathrm{iax},p} \begin{bmatrix}1 & 0 & 0\end{bmatrix}^{\mathrm{T}} + v_{\mathrm{it},p} \begin{bmatrix}0 & 0 & \pm 1\end{bmatrix}^{\mathrm{T}} \tag{15}$$

The sign of the tangential velocity is chosen according to whether the propeller blade induces an up- or downwash at the strip. In contrast to Eq. (14), the effect of rotational rates $\boldsymbol{\omega}^B$ is included in Eq. (15) to consider aerodynamic damping of rotational motion. Based on the resulting velocity, the effective angle of attack $\alpha_{\mathrm{eff},s}$, and the aerodynamic drag, lift, and moment coefficients $c_{D,s}$, $c_{L,s}$, and $c_{M,s}$, can be computed for each strip. The wings both have a GA(W)-2 airfoil, whereas all lateral stabilizers have a symmetric NACA-0009 profile, and coefficients are computed the same way as in [22] Based on [23, 24], the effect of control surface deflection on the respective strip aerodynamics is modeled as an increment in the aforementioned coefficients by:

$$\left(\Delta C_{D\delta}\right)_k = C_{D\delta} \cdot \delta_{e,k} \sin \delta_{e,k} \tag{16}$$

$$\left(\Delta C_{L\delta}\right)_k = C_{L\delta} \cdot \delta_{e,k} \tag{17}$$

$$\left(\Delta C_{M\delta}\right)_k = C_{M\delta} \cdot \delta_{e,k} \tag{18}$$

where the computation of C_{D_δ}, C_{L_δ}, and C_{M_δ} is likewise adopted from [23, 24]. In addition, to capture the effect of flow separation on flap effectiveness, the increment in lift in Eq. (17) is blended in and out with an arctan-function. The resulting lift and drag coefficients are corrected for the finite wing with strip-averaged lift distribution and induced drag. The drag, lift and pitch moment are defined as

$$D_s = \overline{q}_s c_{D,s} S_s, \quad L_s = \overline{q}_s c_{L,s} S_s, \quad M_{y,s} = \overline{q}_s c_{M,s} S_s c_s \tag{19}$$

with strip area S_s, chord c_s, and dynamic pressure at the strip $\overline{q}_s = ||\boldsymbol{v}_s||^2 \rho/2$.

The resulting strip force vector is found as:

$$\boldsymbol{f}_{A,s}^B = \boldsymbol{R}_{\mathrm{bw,i}} \boldsymbol{R}_{\mathrm{wa,s}} \begin{bmatrix} -D & 0 & -L \end{bmatrix}_s^T \tag{20}$$

with rotation matrix $\boldsymbol{R}_{\mathrm{wa,s}}$ from aerodynamic to wing frame, which represents a rotation around the y-axis with angle $\alpha_{\mathrm{eff},s}$.

The gravity and fuselage drag force vectors are found as:

$$\boldsymbol{f}_G^B = m \boldsymbol{R}_{\mathrm{eb}} \begin{bmatrix} 0 & 0 & g \end{bmatrix}^T \tag{21}$$

$$\boldsymbol{f}_F^B = -\left(\boldsymbol{v}^B\right)^T \boldsymbol{v}^B \rho/2 \; S_{\mathrm{wet},F} \; C_f k_p F_F \tag{22}$$

with gravitational acceleration g and transformation $\boldsymbol{R}_{\mathrm{eb}}$ from earth to body frame. The element-wise product $\left(\boldsymbol{v}^B\right)^T \boldsymbol{v}^B$ in Eq. (22) contains the directional information, such that the fuselage drag always acts in direction of the freeflow. The equations for form factor F_F, wetted fuselage area $S_{\mathrm{wet},F}$ and turbulent skin friction coefficient C_f are given in the Appendix A.B. To account for additional parasitric effects and wing/fuselage interference, a correction factor of $k_p = 1.5$ is applied in Eq. (22).

The different aerodynamic model fidelities - 2D from [2], 3D *minimum strip* from this work, and full strip from [22] - are compared in Fig. 2. The plots show the aerodynamic aircraft response as the sum of all aerodynamic components $\boldsymbol{f}_a^B$ and $\boldsymbol{m}_a^B$ over the tilt angle δ_w which are set equal for both wings.

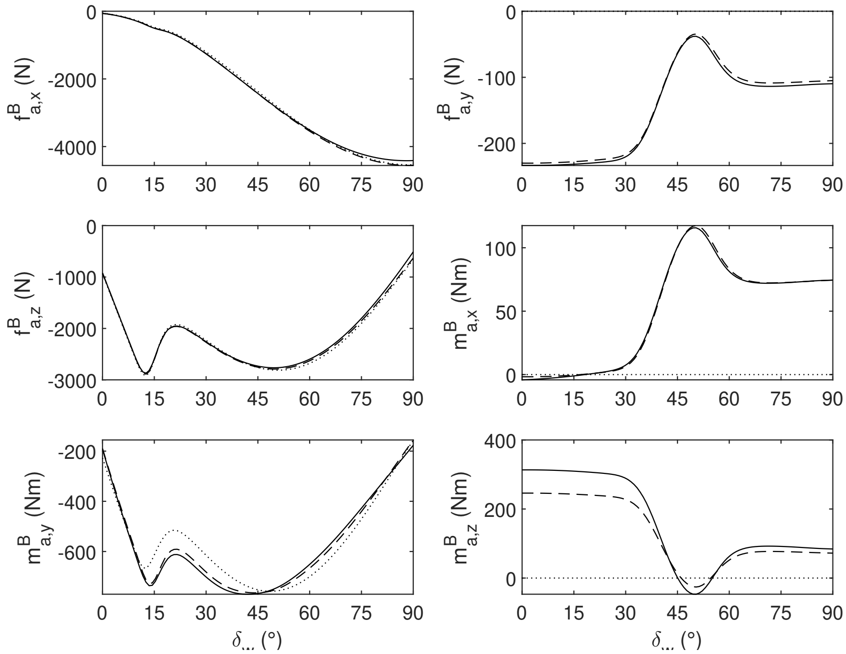

Fig. 2 Aerodynamic response of 2D (·····), 3D (- - -), and full strip theory (——) models for constant axial flight velocity of $V = 25\,\mathrm{m\,s^{-1}}$ and sideslip $\beta = 3°$ at constant thrust settings of $T_p = 375\,\mathrm{N}$ for all rotors.

Obviously, the 2D model gives no lateral response. Other than that, all models show good conformance and predict the same general behavior. However, there is a large deviation in pitch moment for the 2D model between 14° and 45°, which can be traced back to the missing effect of swirl. Thus, the 3D model gives a more accurate result in this region. In contrast, the 3D model shows underpredicted yaw moments $m_{a,z}^B$ throughout the tilt angle range, which results primarily from the simplified model of the *inverted V*.

Note that in optimal control, the system dynamics have to be computed for each point of the time grid, wherefore the model structure is adapted to perform all multiplications element-wise. That way, all time points are computed simultaneously without the use of for-loops, which drastically improves the computation time.

B. Optimal Control Problem Formulation

The aim of optimal control is to find the optimal control inputs $u(t) \in \mathbb{R}^{n_u}$ that bring the system with states $x(t) \in \mathbb{R}^{n_x}$ and dynamics $f : \mathbb{R}^{n_x} \times \mathbb{R}^{n_u} \times \mathbb{R} \to \mathbb{R}^{n_x}$ from its initial state $x_0 = x(t_0)$ to a desired terminal state at $x_f = x(t_f)$, with minimized cost $J : \mathbb{R}^{n_x} \times \mathbb{R}^{n_u} \times \mathbb{R} \to \mathbb{R}$ while complying with path and derivative constraint functions (ϕ_g and ϕ_r). The definition of the initial and terminal states is formulated as boundary constraints ϕ_b. Transferred to the 6DoF tilt-wing model, the state and input vectors are

$$\boldsymbol{x} = \begin{bmatrix} \boldsymbol{r}^E & \boldsymbol{v}^B & \boldsymbol{\theta} & \boldsymbol{\omega}^B & \boldsymbol{\delta}_w \end{bmatrix}^{\mathrm{T}} \tag{23}$$

$$\boldsymbol{u} = \begin{bmatrix} \boldsymbol{t}_P & \boldsymbol{\delta}_{wc} & \boldsymbol{\delta}_e \end{bmatrix}^{\mathrm{T}} \tag{24}$$

with the position vector in the earth frame $\boldsymbol{r}^E$, vector of Euler angles $\boldsymbol{\theta}$, thrust vector $\boldsymbol{t}_P$ for all rotors, and deflection vector $\boldsymbol{\delta}_e$ for all control surfaces. As the tilt actuation $\boldsymbol{\delta}_w$ has low bandwidth, it is modeled as a first-order function of commanded tilt angle deflection $\boldsymbol{\delta}_{wc}$ with time constant $\tau_{\delta_w} = 2$. In contrast, the dynamics of rotors and control surfaces are higher and thus not as crucial for the vehicle behavior, wherefore they are modeled with rate constraints (see Table 2).

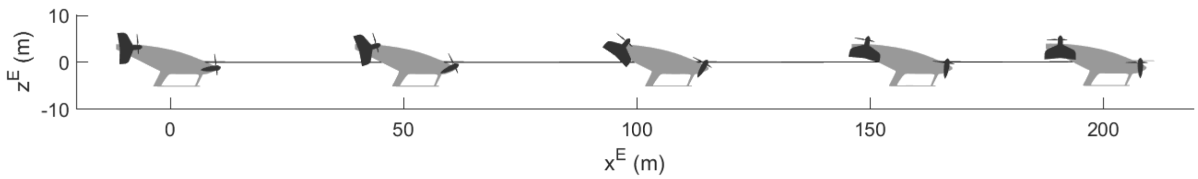

Fig. 3 Side view of upscaled aircraft in level backward transition maneuver.

The goal of the trajectory optimization is to perform a longitudinal level backward transition from cruise to hover flight state (as illustrated in Fig. 3) within a fixed terminal time of $t_f = 20\,\mathrm{s}$. In general, the terminal time can be part of the optimization problem, but a fixed t_f eases the comparison between different failure cases and the nominal maneuver. The chosen terminal time is about twice as high as for the time-optimal level backward transition under nominal conditions. The boundaries for all variables are provided in Table 2 and enforce the desired behavior. Only upward aircraft motion ($0 \leq \dot{z}^E$) is allowed. Together with the objective to minimize the terminal altitude

$$J = z_f^E, \tag{25}$$

the aircraft tries to stay as close as possible to the initial reference altitude, which leads to a level transition ($\Delta z^E \approx 0$). This combination of constraint and objective also prevents the aircraft from descending in hover mode after the transition, which is undesired. The pitch angle θ (as well as the other Euler angles) is constrained to small values to ease the comparison between nominal and failure case. Nevertheless, for cases where the optimization is not successful, the constraint can be loosened up to $\theta \in [-15°, 15°]$. As the backward transition is a decelerating maneuver, accelerations in x^B-direction are avoided with $\dot{u}^B \leq 0$. To avoid chattering in all components of the body moment vector $\boldsymbol{m}^B$, the derivatives of rotational rates $\boldsymbol{\omega}^B$ are constrained to be small. For the thrust command, the lower bound is set to 1 instead of 0 to avoid imaginary results in Eq. (12), as the deployed IPOPT-solver makes use of boundary expansion. Note that empty cells in Table 2 represent unboundedness (implemented with a large number).

State Variables					
Variable	Unit	lower Bound	upper Bound	lower RC	upper RC
x^E	m	0		0	100
y^E	m	-1	1		
z^E	m	0	100	0	
u^B	$\mathrm{m\,s^{-1}}$	0	100	$-0.5g$	0
v^B	$\mathrm{m\,s^{-1}}$	-0.1	0.1		
w^B	$\mathrm{m\,s^{-1}}$	-2	2	$-0.25g$	$0.25g$
$\boldsymbol{\theta}$	°	-0.5	0.5		
$\boldsymbol{\omega}^B$	$°\,\mathrm{s^{-1}}$	$-1\mathrm{e}{-2}$	$1\mathrm{e}{-2}$	$-1\mathrm{e}{-4}$	$1\mathrm{e}{-4}$
$\boldsymbol{\delta}_w$	°	0	90		
Input Variables					
Variable	Unit	lower Bound	upper Bound	lower RC	upper RC
$\boldsymbol{t}_P$	N	1	1125	-1000	1000
$\boldsymbol{\delta}_{\mathrm{wc}}$	°	0	90	-45	45
$\boldsymbol{\delta}_e$	°	-30	30	-90	90
Time Variable					
Variable	Unit	lower Bound	upper Bound	lower RC	upper RC
t_f	s	20	20		

Table 2 State, input, and time variables of the optimal control problem and their respective boundaries and rate constraints (RC).

In former work [2], we found transition trajectories between trimmed cruise and hover flight conditions, meaning that the trim points were found beforehand and introduced as variable bounds of $\boldsymbol{x}$ and $\boldsymbol{u}$ for the optimization. For an over-actuated aircraft like the tilt-wing, these trim points are not unique and leave freedom to be chosen more or less freely, e.g. to minimize an objective function. However, the chosen trim states have a strong impact on the solution of the trajectory optimization. While this is no issue for nominal trajectory optimization, for failure conditions instead, the trim points also influence whether feasible trajectories can be found at all. In case of the backward transition, this counts especially for the terminal time point where the hover state requires high trust settings which cannot be established instantaneously. It was found that the vehicle would often perform a reallocation during the transition to comply with the enforced trim hover state and that - depending on the failure scenario - the reallocation could not always be accomplished (in time). Therefore, the hover point is not trimmed in advance, but instead as part of the trajectory optimization by enforcing zero state derivatives at terminal time:

$$-1\text{e}{-4} \leq \dot{\boldsymbol{x}}_f \leq 1\text{e}{-4} \tag{26}$$

As the propellers operate at low thrust in cruise, constraining the initial time point to trimmed cruise flight conditions is not as limiting. However, the trim requirement might not be fulfilled for all failure combinations, so unsteady initial conditions (within the limits of Table 2) are accepted in the solution. Apart from that, the cruise velocity is defined to be $u^B = 40\,\text{m}\,\text{s}^{-1}$, and hover has, of course, zero flight speed $\boldsymbol{v}^B = \boldsymbol{0}$.

To obtain a nonlinear program (NLP) that can be solved with a gradient-based solver, the system dynamics are transcribed with trapezoidal collocation on a grid with 61 nodes. Despite the large number of states and inputs (14 respectively) and the resulting high-dimensional optimization space, the optimal control framework shows robust convergence without a requirement for complex initialization.

III. Trajectory Optimization Results

The trajectory optimization from the previous section is now applied for the investigation of the backward transition maneuver. To give some insights on the general tilt-wing transition characteristics, first a nominal transition is considered before an encompassing investigation of single and combined failure cases is performed.

A. Nominal Backward Transition

For the intended level longitudinal backward transition, the aircraft has to balance all forces and moments, except the horizontal force (which is equal to f_x^B) used for deceleration. Thus, the results in Fig. 4 do not show states except the longitudinal velocity in body frame u^B (which is redundant to position x^B), as they are zero anyway, and the focus instead is on the actuation. In the wing-borne cruise state at $40\,\text{m}\,\text{s}^{-1}$, thrust settings are almost at idle and both wing deflections are close to zero. Accordingly, as shown in Fig. 5(a), aerodynamic forces (in grey) are dominant over propulsive forces (in blue). The resulting total force vectors at both wings are slightly tilted forward causing a positive force. However, the fuselage drag $\boldsymbol{f}_F$ causes decelerating conditions. In cruise and early transition (until $t \approx 8\,\text{s}$), differential wing deflection is applied to balance the pitching moment. The CG is slightly shifted towards the main wing, wherefore the vertical force at the main wing (subscript m) has to be slightly larger ($\approx 5.5\%$) than at the canard wing (subscript c) to balance the pitching moment. In cruise, this is inherently obtained, as the surface area of the main wing and thus the aerodynamic lift is larger. Consequently, differential tilt angles with higher deflections at the canard wing are commanded. The canard thus initiates the backward transition maneuver, whereas the main wing follows. In early backward transition, we can observe the typical non-linear behavior (described in [2, 22, 25, 26] when entering into flow separation. In the second part of the transition maneuver, both tilt angles assume similar deflections and pitch is balanced with differential thrust, where the thrust force has to be larger now at the main wing to compensate for the shorter lever arm to the CG. With increased thrust settings, propeller-wing interactional effects increase, and there is an induced aeodynamic force in negative x^B-direction, see Fig. 5(b). The propeller-induced lift is larger for the inboard wing section and decreases towards the wing tips, according to the assumed elliptical lift distribution. As the induced lift serves as a decelerating force, the inner rotors (T_2 and T_3 at main wing as well as T_6 and T_7 at canard) run at higher thrust. This effect in combination with increased control surface deflections for deflected slipstream would be even more exploited for time-optimal trajectories. In steady hover flight, next to all other forces and moments, also the total longitudinal force f_x^B has to be zero, which is achieved by a slightly forward tilted thrust vector to compensate for the induced lift in negative direction (see Fig. 5(b)).

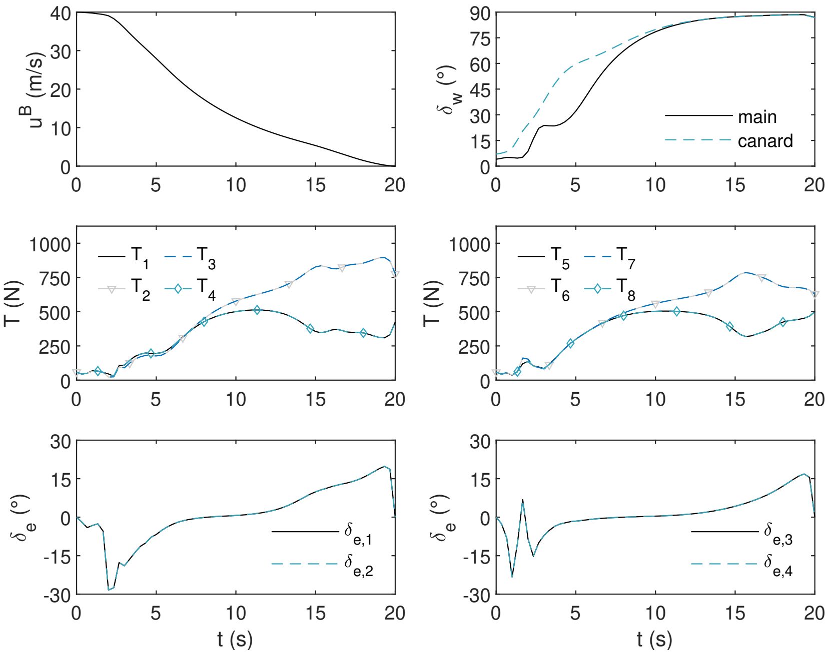

Fig. 4 Result of trajectory optimization for longitudinal level backward transition under nominal conditions.

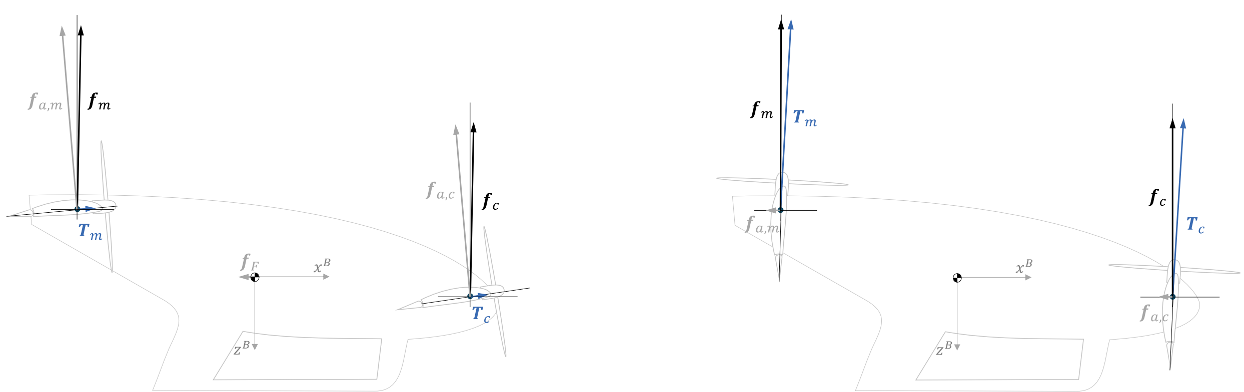

(a) Cruise state at t_0

(b) Hover state at t_f

Fig. 5 Aero-propulsive forces in cruise and hover state under nominal conditions.

B. Failure Cases

There are various forms of potential failure sources for an eVTOL aircraft. For an initial investigation, it makes sense to investigate the actuation system of the vehicle by considering failures of propulsion and/or control surfaces. In contrast, failure of the tilt actuation is not considered, as this would impede the transition and therefore require substantially different landing strategies. Aiming for the strongest impact on flight performance, complete losses of rotors or runaways of control surfaces are considered. These can be easily introduced into the problem formulation by adapting the variable limits. For rotor p, this leads to

$$1 \leq T_p \leq 1 \tag{27}$$

where the boundaries of 1 are used again to avoid complex results in Eq. (12). For control surface runaways, it is not clear which direction of runaway has the strongest effect on flight performance, wherefore both negative and positive deflection limits, denoted by $\delta^-_{e,k}$ and $\delta^+_{e,k}$, are tested:

$$\delta_{e,\min} \leq \delta^-_{e,k} \leq \delta_{e,\min} \ , \ \delta_{e,\max} \leq \delta^+_{e,k} \leq \delta_{e,\max} \tag{28}$$

with $\delta_{e,\min} = -30°$ and $\delta_{e,\max} = 30°$.

With the ambition to investigate all cases of single failure and combinations of two failing components, the symmetry of the aircraft is exploited to reduce the number of test cases. Therefore, for failure 1 only components on the right side of the aircraft are considered, whereas failure 2 can assume all forms of rotor losses or runaways. The resulting test matrix is shown in Table 3 and indicates for each failure combination if the initial cruise $\boldsymbol{x}_0$ and terminal hover $\boldsymbol{x}_f$ conditions can be trimmed, and if the trajectory optimization converged successfully (1 indicating success). Empty cells represent obvious symmetric test cases, and the diagonal where the same variables for failure 1 and failure 2 meet (from T_1T_1 to $\delta^+_{e,3}\delta^+_{e,3}$) represents single failure.

<table>
<tr><th></th><th></th><th colspan="8">Failure 1</th></tr>
<tr><th></th><th></th><th>T_1</th><th>T_2</th><th>T_5</th><th>T_6</th><th>$\delta^-_{e,1}$</th><th>$\delta^+_{e,1}$</th><th>$\delta^-_{e,3}$</th><th>$\delta^+_{e,3}$</th></tr>
<tr><td rowspan="16">Failure 2</td><td>T_1</td><td>1|1|1</td><td>-</td><td>-</td><td>-</td><td>-</td><td>-</td><td>-</td><td>-</td></tr>
<tr><td>T_2</td><td>1|0|0</td><td>1|1|1</td><td>-</td><td>-</td><td>-</td><td>-</td><td>-</td><td>-</td></tr>
<tr><td>T_5</td><td>1|0|0</td><td>1|1|1</td><td>1|1|1</td><td>-</td><td>-</td><td>-</td><td>-</td><td>-</td></tr>
<tr><td>T_6</td><td>1|1|1</td><td>1|1|1</td><td>1|0|0</td><td>1|1|1</td><td>-</td><td>-</td><td>-</td><td>-</td></tr>
<tr><td>$\delta^-_{e,1}$</td><td>1|1|1</td><td>1|1|1</td><td>1|1|1</td><td>1|1|1</td><td>1|1|1</td><td>-</td><td>-</td><td>-</td></tr>
<tr><td>$\delta^+_{e,1}$</td><td>1|1|1</td><td>1|1|1</td><td>1|1|1</td><td>1|1|1</td><td>1|1|1</td><td>1|1|1</td><td>-</td><td>-</td></tr>
<tr><td>$\delta^-_{e,3}$</td><td>1|1|1</td><td>1|1|1</td><td>1|1|1</td><td>1|1|1</td><td>1|1|1</td><td>1|1|1</td><td>1|1|1</td><td>-</td></tr>
<tr><td>$\delta^+_{e,3}$</td><td>1|1|1</td><td>1|1|1</td><td>1|1|1</td><td>1|1|1</td><td>1|1|1</td><td>0|1|0</td><td>1|1|1</td><td>1|1|1</td></tr>
<tr><td>T_3</td><td>1|0|0</td><td>1|0|0</td><td>1|1|1</td><td>1|1|1</td><td>1|1|1</td><td>1|1|1</td><td>1|1|1</td><td>1|1|1</td></tr>
<tr><td>T_4</td><td>1|0|0</td><td>1|0|0</td><td>1|1|1</td><td>1|1|1</td><td>1|1|1</td><td>1|1|1</td><td>1|1|1</td><td>1|1|1</td></tr>
<tr><td>T_7</td><td>1|1|1</td><td>1|1|1</td><td>1|1|1</td><td>1|1|1</td><td>1|1|1</td><td>1|1|1</td><td>1|1|1</td><td>1|1|1</td></tr>
<tr><td>T_8</td><td>1|1|1</td><td>1|1|1</td><td>1|1|1</td><td>1|1|1</td><td>1|1|1</td><td>1|1|1</td><td>1|1|1</td><td>1|1|1</td></tr>
<tr><td>$\delta^-_{e,2}$</td><td>1|1|1</td><td>1|1|1</td><td>1|1|1</td><td>1|1|1</td><td>1|1|1</td><td>0|1|0</td><td>1|1|1</td><td>1|1|1</td></tr>
<tr><td>$\delta^+_{e,2}$</td><td>1|1|1</td><td>1|1|1</td><td>1|1|1</td><td>1|1|1</td><td>0|1|0</td><td>1|1|1</td><td>1|1|1</td><td>1|1|1</td></tr>
<tr><td>$\delta^-_{e,4}$</td><td>1|1|1</td><td>1|1|1</td><td>1|1|1</td><td>1|1|1</td><td>1|1|1</td><td>1|1|1</td><td>1|1|1</td><td>1|1|1</td></tr>
<tr><td>$\delta^+_{e,4}$</td><td>1|1|1</td><td>1|1|1</td><td>1|1|1</td><td>1|1|1</td><td>1|1|1</td><td>1|1|1</td><td>1|1|1</td><td>1|1|1</td></tr>
</table>

Table 3 Test matrix showing if a solution for (trim of $\boldsymbol{x}_0$ | trim of $\boldsymbol{x}_f$ | trajectory optimization) is found for backward transition maneuver under different failure combinations.

All failure scenarios with unsuccessful backward transition trajectory optimization are highlighted. While this alone does not necessarily mean that the transition is impossible under the respective conditions, it gives a first indication of challenging failure combinations. The highlighted test cases can be categorized into either combined rotor failures or combined control surface runaways. In contrast, for all mixed rotor-runaway failure combinations, a solution is found. For the highlighted combined control-surface failures, no trim point can be found in cruise conditions at $\boldsymbol{x}_0$. This does not imply that the transition is infeasible, as trimmed initial conditions are not required. Instead, for unsuccessful rotor combinations, no hover trim solution at $\boldsymbol{x}_f$ is found, which suggests that a transition indeed is no longer possible, as we require the trajectory to terminate in trimmed hover conditions (Eq. (26)). In the following, the critical failure combinations are investigated in more detail. Note that T_1T_3 and T_2T_4, as well as $\delta^-_{e,1}\delta^+_{e,2}$ and $\delta^+_{e,1}\delta^-_{e,2}$, are equivalent test cases due to symmetry, and only one case is considered respectively.

IV. Detailed Analysis of Critical Cases

This subsection investigates why the trajectory optimization failed for the highlighted test cases in Table 3, and tries to verify if the backward transition under these conditions is indeed not feasible any longer.

A. Combined Rotor Failures

All unsuccessful combined rotor failures, illustrated in Fig. 6, have in common that no trim point in hover conditions can be found. This means that the backward transition maneuver as defined in Section II.B is indeed impeded, and the transition analysis can be reduced to the investigation of why there exists no trim point for the hover state. For trimming

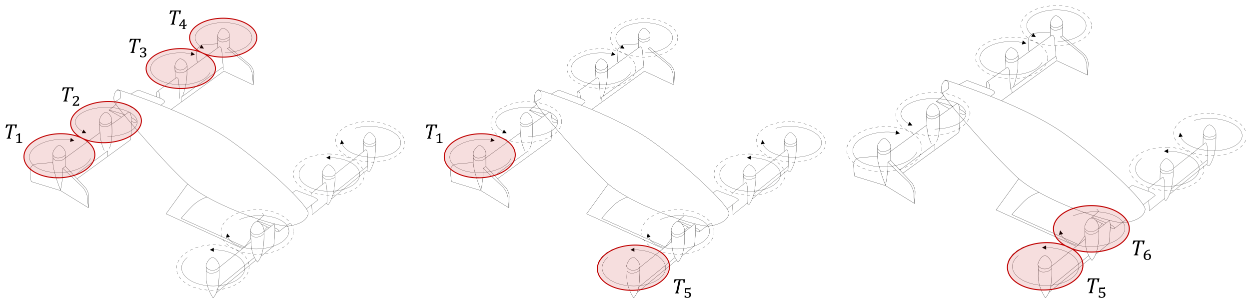

(a) T_1T_2, T_1T_3, T_1T_4, T_2T_3 (b) T_1T_5 (c) T_5T_6

Fig. 6 Overview of critical combinations for two simultaneous rotor failures.

in hover conditions, all state derivatives shall be zero, which is equivalent to $\boldsymbol{f}^B = \boldsymbol{0}$ and $\boldsymbol{m}^B = \boldsymbol{0}$. Obviously, not all constraints can be fulfilled at the same time for the considered cases. If we loosen one constraint - meaning one component of either $\boldsymbol{f}^B$ or $\boldsymbol{m}^B$ - and instead replace the constraint for this component by a minimization objective for its absolute value, we obtain the deficits shown in Table 4 for vertical lifting force f_z^B or pitching moment m_y^B, if all other forces and moments remain constrained.

Failure case	T_1T_2	T_1T_3	T_1T_4	T_2T_3	T_1T_5	T_5T_6
Δf_z^B (N)	516.5	180.9	135	171.7	154.7	22.4
Δm_y^B (N m)	1081.5	320.3	238.6	303.7	n.f.	−97.4

Table 4 Deficits Δ for vertical force f_z^B and pitching moment m_y^B when loosening the respective hover trim constraint.

Table 4 confirms that lift and pitch moment constraints can never be fulfilled together - otherwise, there would not remain a deficit. For all these cases, the constraints on roll and yaw moment m_x^B and m_z^B require cutting down the thrust of corresponding rotor pairs, leaving merely four rotors fully operational - two on the main and two on the canard wing, respectively. With a thrust-to-weight ratio of close to 2 (1.93 in nominal conditions), all four fully available rotors have to be operated close to the maximum thrust to provide sufficient lift. However, as the CG is shifted slightly towards the main wing by design, the total vertical force has to be larger at the main wing than at the canard wing to balance pitch. Thus, for all combined rotor failures on the main wing (T_1T_2, T_1T_3, T_1T_4, T_2T_3, see Fig. 6(a)), either the pitching moment of the main wing cannot be balanced (positive pitch moment in Table 4), or the lifting force is too small (positive force in body z-direction).

This is demonstrated for the example of T_1T_2 (Fig. 7) when looking at the resulting inputs $\boldsymbol{u}$ in Table 5 corresponding to the loosened constraint trim analysis from Table 4. When T_1 and T_2 fail, the corresponding diagonal rotors T_7 and T_8 (grey in Fig. 7) have to be operated at low thrust settings to allow balancing the lateral moments. If the vertical force f_z^B is not constrained but minimized, the pitch moment still has to be balanced. Thus, the vertical force at the main wing has to be higher than at the canard wing (due to the lever arm), wherefore T_7 is cut down completely and T_6 cannot be operated at full thrust. If instead the pitch balance constraint is loosened, these rotors can provide more thrust to fulfill $f_z^B = 0$, which, however, unbalances the pitching moment.

The failure case of both outer rotors on the right side T_1T_5 (Fig. 6(b)), in contrast, is special, as it never allows to

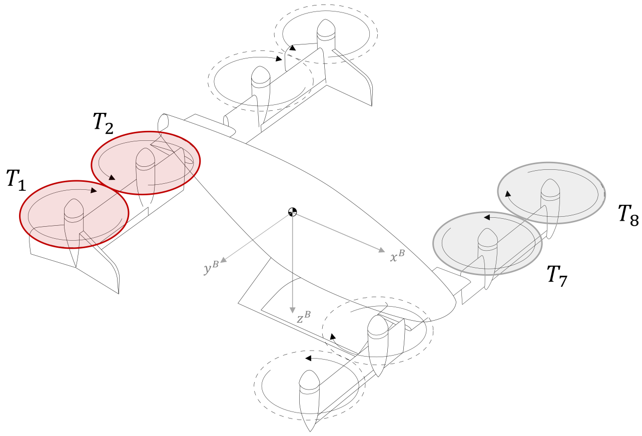

Fig. 7 Combined failure for rotors T_1T_2.

Actuator	Δf_z^B	Δm_y^B
T_1(N)	1	1
T_2(N)	1	1
T_3(N)	1125	1125
T_4(N)	997	959
T_5(N)	1125	1125
T_6(N)	895	1125
T_7(N)	1	324.3
T_8(N)	1	1
$\delta_{w1}(^\circ)$	85.2	85.1
$\delta_{w2}(^\circ)$	85.5	85.5
$\delta_{e1}(^\circ)$	−16.85	−13.7
$\delta_{e2}(^\circ)$	30	30
$\delta_{e3}(^\circ)$	30	27
$\delta_{e4}(^\circ)$	30	30

Table 5 Trim inputs $\boldsymbol{u}$ for loosened constraints in hover state for failure of T_1T_2.

fulfill the f_z^B-requirement (n.f. for not feasible). This is again caused by the yaw and roll moment requirements, which demand to completely cut down the outer rotors on the left side $T4$ and $T8$. In addition, the canard wing is deflected vertically for pitch control. At the same time, both wings induce a high lift component in negative x^B-direction due to elliptical lift distribution at the inner sections. As it was mentioned for the nominal case in Fig. 5(b), this force has to be canceled by tilting the thrust vector (here at the main wing) forward, which in consequence reduces the available lifting force.

If two rotors at the canard fail on the same half-wing (T_5T_6, see Fig. 6(c)), more lifting thrust force can be provided at the main wing than at the canard to fulfill the f_z^B-constraint, resulting in a negative pitching moment. Instead, to balance the pitching moment, thrust is reduced at the main wing (T_3) and shifted to the canard wing (T_8), but this reduces the total vertical force and there remains a deficit in f_z^B.

As the considered failure conditions do not allow to harmonize lifting force and pitch moment requirements, one might consider relaxing the pitch angle constraint to improve the pitch balance. For passenger-friendly limits of $\theta \in [-15^\circ, 15^\circ]$, there is a small improvement in pitching moment deficit. However, pitch angles above 70° are required to allow trimming for the cases T_1T_2, T_1T_3, and T_1T_4. If instead the thrust-to-weight ratio is increased to improve hover trim conditions for these cases, only T_5T_6 becomes trimmable, which had the smallest deficits in Table 4. Note that additional thrust is often limited by design.

Next to changes in operation or design, Table 6 shows for which conditions trimming becomes feasible again if the extent of the rotor failure is lowered from a full loss to a reduction of maximum available thrust (in percent of nominal max. thrust $T_{\max}$). Here, the same upper limits for both failed rotors are assumed. For all cases, transition trajectory optimization is feasible as soon as steady-state hover conditions can be achieved.

Failure case	T_1T_2	T_1T_3	T_1T_4	T_2T_3	T_1T_5	T_5T_6
Reduced failures 1 & 2	6.1	4.1	3.7	3.9	3.3	0.5

Table 6 Required percentage of nominal maximum thrust $T_{\max}$ to trim hover state under failure conditions.

B. Combined Control Surfaces Failures

The second category of failures with a critical impact on backward transition are combined control surface runaways. Instead of the hover trim point in Section IV.A, here no steady-state cruise flight conditions can be found. In general, that is no problem as long as the lateral motion can be balanced, as trimmed initial conditions are not required for x_0 in the trajectory optimization. However, lateral motion is indeed unbalanced in cruise conditions for the case $\delta^-_{e,1}, \delta^+_{e,2}$, where both control surfaces at the main wing are deflected in opposite directions. In cruise flight, the thrust settings are low and cannot be increased as positive accelerations $\dot{u}^B$ are constrained (see Table 2). Thus, thrust forces cannot be deployed to balance the lateral moments. Above that, the main wing aerodynamics are dominant over the canard wing due to the larger surface area. Therefore, it is not possible to counter the lateral disturbances introduced at the main wing by opposed surface deflections at the canard wing. For decreased cruise flight speeds, however, the aerodynamic response is reduced, and lateral moments can be balanced with combined canard control surface deflections and differential thrust settings. Below $37\,\mathrm{m\,s^{-1}}$, cruise flight trimming as well as the complete backward transition become feasible again.

The other critical control surface failure case is found for positive deflections of both surfaces on the same side of the aircraft, here $\delta^+_{e,1}, \delta^+_{e,3}$. Again, trimming is not successful in cruise flight conditions. While the lateral disturbances due to the respective control surface runaways can be canceled with symmetric deflections on the opposite side, this lets all surfaces act like high-lift devices, wherefore the vertical aircraft motion is not in steady state. While this does not contradict the problem formulation, the backward transition fails because the deceleration capability is limited, and thus larger times for the maneuver are required. Trajectories can be found for terminal times $t_f \geq 29.4\,\mathrm{s}$, as shown in Fig. 8. The observed control inputs in the plots explain why the transition takes longer: Around cruise conditions, the lateral motion is balanced with symmetric control surface deflections on the opposite side ($\delta_{e,2}, \delta_{e,4}$). However, with increased tilt angle deflections, this would no longer allow balancing the pitching moment, wherefore now differential thrust instead of control surface deflections is deployed to counter the disturbances. Compared to the nominal case, this requires higher thrust settings which lowers deceleration capabilities. Next to an extended time for the maneuver, another option to facilitate transition is to release the pitch motion, where $\theta \in [-5°, 5°]$ is already sufficient to comply with the originally required terminal time of 20 s. Again, as observed in the nominal case in Fig. 4, the conditions in early transition are challenging, and chattering occurs in the thrust commands in Fig. 8

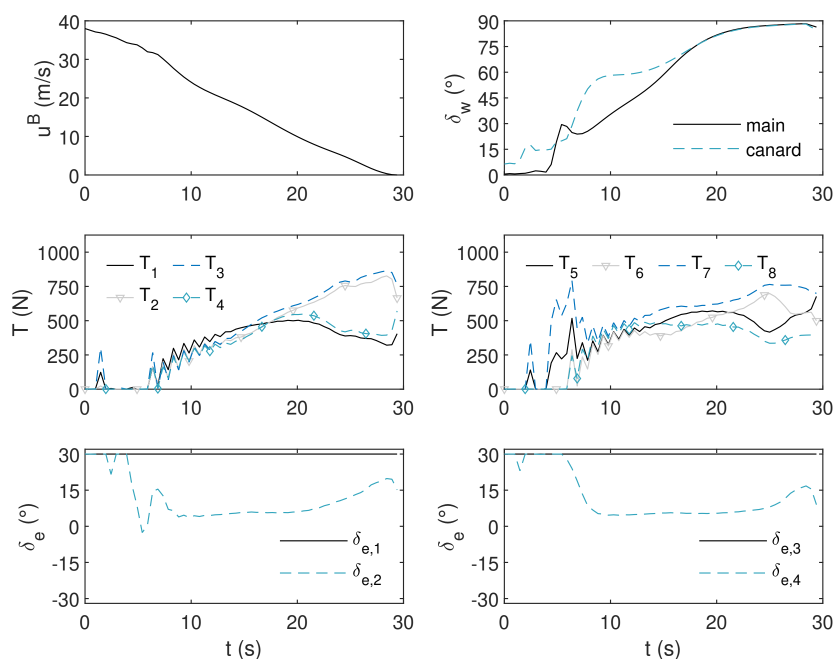

Fig. 8 Result of trajectory optimization for longitudinal level backward transition under combined control surface failure for $\delta^+_{e,1}, \delta^+_{e,3}$, with t_f = 29.4 s.

V. Discussion

This research aims to assess the remaining backward transition capability of a tilt-wing aircraft under failure conditions. The deployed optimal control framework allows to identify challenging failure scenarios and provides insights into the respective failure-handling strategy. Compared to similar research, the trajectory optimization is based on a complex 6DoF model that covers 3D propeller-wing interaction. This results in a large and computationally intensive optimization problem. Still, the convergence is robust and the framework does not require complex initialization procedures, even when introducing failure conditions. In addition, the model and framework are adapted to reduce the computational burden, and computation time is about a minute per case (on a business notebook). This allows the investigation of numerous failure combinations in acceptable time. In contrast to static trim analyses, the OC approach allows to include dynamic (e.g., inertial) effects, and thus gives a more accurate estimation of the remaining flight performance. If a feasible trajectory for the transition maneuver is found, this is sufficient to state that transition is still possible under these failure conditions. In contrast, an unsuccessful optimization does not serve as a sufficient criterion to state the opposite. This is mostly due to the gradient-based solver, which might get stuck in local regions of the solution space and thus does not investigate all existing possibilities. Consequently, a detailed subsequent analysis of those failed test cases is required. Nevertheless, all identified critical failure combinations in this work did indeed no longer allow to perform the backward transition.

Next to the method, also the test scenario can be discussed. To the author's knowledge, this is the first investigation for eVTOLs that considers failure combinations of different (propeller and control surface) failures, whereas most other research is limited to single engine failures. Thereby, this work addresses the vehicle design which is typically characterized by a strong overactuation. Nevertheless, for a thorough vehicle assessment, other hazards or stepwise degradation of components should be taken into account. To assess the remaining flight performance of the tilt-wing, only the backward transition maneuver is investigated. This results from the observation in former work that the backward transition is the most challenging flight phase for the considered tilt-wing aircraft, which can probably be transferred to similar vehicle configurations. Therefore, the backward transition represents the bottleneck of flight performance, also because this maneuver is required to allow for a safe (vertical) landing. In the test setup, the aircraft motion is further constrained to level longitudinal flight with all Euler angles at zero, primarily to allow a comparison of failure cases against nominal behavior. Yet, in emergency situations, also other forms of transition and landing maneuvers would probably be considered acceptable. For example, some of the identified critical failure conditions suffered from impeded hover capabilities which would always result in descending flight states. However, if this descent rate is limited, it might still be acceptable as a backup for emergency landings, as the example of helicopter autorotation shows. Next to that, failure cases might also motivate unconventional transition maneuvers, i.e. a *crabbed* transition (with roll, yaw, and sideslip angles), or a *tailsitter* transition that uses the pitch angle instead of tilt angle deflections, as this allowed to successfully balance the pitching moment for some of the critical failure cases.

Despite the limitations of the test setup, the results give valuable initial insights into the tilt-wing's behavior in failure scenarios. Concerning the aircraft's robustness, the tilt-wing holds the promise of a high level of redundancy. The single failure criterion is fulfilled for all control surface and propulsion failures, which show no significant impact on backward transition performance. For combinations of two failures, most scenarios still allow a successful transition. The critical failure cases can be categorized into either combined rotor or combined control surface failures. All propulsion-related critical cases suffered from unbalanced hover conditions. If the conditions were improved (i.e. the extent of failure was reduced), transition trajectories were found again as soon as hover flight could be balanced. In contrast, for a positive runaway of control surfaces on the same side of canard and main wing, the transition capability itself was the limiting factor. This is interesting for the intended estimation of the transition corridor in the future, as there seems to appear a gap in the corridor between hover and cruise conditions for this failure case. Above that, the results provide some guidelines for vehicle design, as critical design aspects are highlighted from a flight mechanic perspective. For example, it was observed that backward transition is no longer possible if the rotors on the same half-wing fail. However, e.g., power supply and signal cables of these rotors pass the same sensitive junction between fuselage and tiltable wing. Accordingly, the cable routing should consider the criticality of this combined propulsion failure to achieve a not just redundant but resilient design.

VI. Conclusion & Outlook

This paper provides an initial investigation of the remaining tandem tilt-wing backward transition capabilities under various single and combined actuator failures in form of full rotor losses and control surface runaways. The failure conditions are tested on a longitudinal level backward transition. For this, 6DoF trajectory optimization within an optimal control approach is deployed. To consider the asymmetric flight conditions introduced by the failures, a 3D aerodynamic model is developed that uses the minimum number of strips to still capture the effect of propeller swirl on lift distribution. The results give valuable insights into remaining vehicle performance and optimal reallocation strategies. The results indicate the fault tolerance of the tandem tilt-wing aircraft, as transition is still possible for all single failures and most of the combined failure cases. Critical failure combinations are either of the category of combined rotor failures or combined control surface failures, where steady-state hover and cruise conditions prove to be limiting. For the propulsion-dominant cases, the lateral disturbances due to rotor failures impede the harmonization of lift and pitching moment requirements. In wing-borne cruise flight, control surface runaways cause large aerodynamic disturbances that either unbalance the lateral motion, or the control surfaces act like high-lift devices enforcing an upward motion. For the former, increased thrust settings throughout the transition are required to balance the disturbances, wherefore the transition time increases.

The presented work is intended as a foundation for future estimation of the tilt-wing transition corridor for nominal and failure conditions. The corridor estimation, which was already presented in [27] for nominal aircraft behavior, will be conducted in the future on the critical failure combinations identified in this paper. To support that, it could help to test other transition strategies under failure conditions next to the chosen level longitudinal backward transition.

A. Appendix

A. Average swirl velocity at a strip

The index for the respective propeller p is dropped, as all propellers have the same geometry and the computation is equal for all of them. According to [28], the axial force distribution f_x can be related to the tangential force distribution, assuming that the propeller sections do not stall.

$$f_t = f_x \frac{v_x^W + v_{\text{iax}}(r)}{\Omega r} \tag{29}$$

where $v_{\text{iax}}(r)$ is the axially induced velocity at radial position r in the propeller plane, and Ω is the rotational speed defined as $\Omega = 2\pi n$. Based on the change of momentum in the tangential direction, the induced tangential velocity can be obtained as:

$$\tilde{V}_{\text{it}}(r) = \frac{f_t}{2\pi r} \frac{1}{\rho \left(v_x^W + v_{\text{iax}}(r)\right)} \tag{30}$$

$$= \frac{f_x}{2\pi r} \frac{1}{\rho \Omega r} \tag{31}$$

$$= \frac{15}{8\rho} \frac{T}{R - R_{\text{i}}} \hat{r}\sqrt{1-\hat{r}} \frac{1}{\pi r^2 \Omega} \tag{32}$$

, where the radial distribution of f_x is approximated by the Goldstein optimum distribution [29]

$$f_x = \tilde{F}\,\hat{r}\sqrt{(1-\hat{r})} \tag{33}$$

The non-dimensional radial position is defined as

$$\hat{r} = \frac{r - R_{\text{i}}}{R - R_{\text{i}}} \tag{34}$$

with r being the radial position with respect to the propeller axis, R_{i} the root cutout due to the hub, and R the outer propeller radius. The reference value $\tilde{F}$ is obtained by ensuring equality of total thrust T and the integral of the axial load distribution:

$$\tilde{F}\int_0^1 \hat{r}\left(1-\hat{r}\right)^n\left(R-R_{\mathrm{i}}\right)=T \tag{35}$$

$$\Longrightarrow \tilde{F}=\frac{1}{n^2+3n+2}\frac{T}{R-R_{\mathrm{i}}} \tag{36}$$

$$\tilde{F}=\frac{15}{4}\frac{T}{R-R_{\mathrm{i}}} \tag{37}$$

Eq. (32) allows to obtain the radial velocity distribution as a function of r and T/Ω, but the radial distribution of this model is restricted to the range between the propeller cone and outer diameter, and zero outside this range. However, Veldhuis [30] mentions that the swirl effect is not limited to the slipstream tube, wherefore the model by Vatistas et al. [31] with $\hat{n}=2$ is used for the radial distribution:

$$\hat{V}_{\mathrm{it}}=\frac{\Gamma_v}{2\pi r_m}\left\{\frac{\overline{r}}{\left(1+\overline{r}^{2\hat{n}}\right)^{1/\hat{n}}}\right\} \tag{38}$$

$$\overline{r}=\frac{r}{r_m} \tag{39}$$

The vorticity Γ_v can be replaced with the maximum tangential velocity $\tilde{V}_{\mathrm{it,max}}$ if the viscous core radius r_m is inserted into Eq. (32):

$$\frac{\Gamma_v}{2\pi r_m}=\tilde{V}_{\mathrm{it,max}}=\tilde{V}_{\mathrm{it}}\left(r_m\right) \tag{40}$$

The radial position of the maximum of the distribution in Eq. (38) is located at

$$r_m=\frac{3R_{\mathrm{i}}+2R}{2}-\sqrt{\left(\frac{3R_{\mathrm{i}}+2R}{2}\right)^2-4R_{\mathrm{i}}R} \tag{41}$$

Now, the radial distribution can be averaged for all strips on a half-wing. For a strip located within the propeller radius R, this yields

$$\overline{v}_{\mathrm{it}}=\left(\frac{15}{8\rho\left(R-R_{\mathrm{i}}\right)}\frac{\hat{r}_m\sqrt{1-\hat{r}_m}}{\pi r_m^2}\right)\left(\int_0^R\frac{\overline{r}}{\sqrt{1+\overline{r}^4}}d\overline{r}\right)\frac{T}{\Omega} \tag{42}$$

$$=\underbrace{\frac{15}{8\rho\left(R-R_{\mathrm{i}}\right)}\frac{\hat{r}_m\sqrt{1-\hat{r}_m}}{\pi r_m^2}\frac{1}{\overline{R}}\cdot\frac{\log\left(\sqrt{\overline{R}^4+1}+\overline{R}^2\right)}{2}\frac{\sqrt{c_T\rho\left(2R\right)^4}}{2\pi}}_{\overline{c}_{\mathrm{vit}}}\sqrt{T} \tag{43}$$

, where $\hat{r}_m$ is found by inserting r_m into Eq. (34), and $\overline{R}$ is found when inserting $r=R$ into Eq. (39). In the term T/Ω, we replace Ω with the definition for rotor thrust coefficient $T=c_T\rho D^4n^2$ with $D=2R$ and $\Omega=2\pi n$. To obtain results with better conformance to experimental data, [30] recommends to reduce the swirl effect by applying a swirl recovery factor of c_{SRF}. Here, $c_{\mathrm{SRF}}=0.2$ is chosen.

$$\overline{v}_{\mathrm{it}}=\underbrace{\overline{c}_{\mathrm{vit}}c_{\mathrm{SRF}}}_{c_{\mathrm{vit}}}\sqrt{T} \tag{44}$$

B. Fuselage Drag

The form factor of the fuselage is adopted from Torenbeek [32] as:

$$F_F=1+\frac{2.2}{\lambda_F^{1.5}}+\frac{3.8}{\lambda_F^3} \tag{45}$$

where the fuselage fineness ratio $\lambda_F = l_F/d_F$ is defined as the ratio between fuselage length l_F and diameter d_F. According to [32], the fuselage wetted area is found as

$$S_{\text{wet},F} = \pi d_F l_F \left(1 - \frac{2}{\lambda_F}\right)^{2/3} \left(1 + \frac{1}{\lambda_F}\right) \tag{46}$$

, and the turbulent skin friction coefficient is given in [33] as

$$C_f = \left(\frac{1}{3.46 \cdot \log(Re) - 5.6}\right)^2, \; Re = \frac{||\boldsymbol{v}^B|| l_F}{\nu} \tag{47}$$

as a function of Reynolds Number Re with kinematic viscosity ν.

References

[1] Michaelsen, O. E., and Martin, J. F. (eds.), *The Aerodynamic Approach to Improve Flying Qualities of Tilt-Wing Aircraft*, 1963. https://doi.org/10.2514/6.1963-484.

[2] May, M., Milz, D., and Looye, G., "Transition Strategies for Tilt-Wing Aircraft," *AIAA SciTech 2024*, 2024.

[3] Pradeep, P., and Wei, P., "Energy Optimal Speed Profile for Arrival of Tandem Tilt-Wing eVTOL Aircraft with RTA Constraint," *2018 IEEE CSAA Guidance, Navigation and Control Conference (CGNCC)*, IEEE, 2018, pp. 1–6. https://doi.org/10.1109/GNCC42960.2018.9018748.

[4] Doff-Sotta, M., Cannon, M., and Bacic, M., "Fast Optimal Trajectory Generation for a Tiltwing VTOL Aircraft with Application to Urban Air Mobility," *2022 American Control Conference (ACC)*, IEEE, 2022, pp. 4036–4041. https://doi.org/10.23919/acc53348.2022.9867852.

[5] Chauhan, S. S., and Martins, J. R. R. A., "Tilt-Wing eVTOL Takeoff Trajectory Optimization," *Journal of Aircraft*, Vol. 57, No. 1, 2020, pp. 93–112. https://doi.org/10.2514/1.C035476.

[6] Panish, L., and Bacic, M., "Tiltwing eVTOL Transition Trajectory Optimization," *Journal of Aircraft*, 2024, pp. 1–13. https://doi.org/10.2514/1.c037862.

[7] Lu, Z., Hong, H., and Holzapfel, F., "Multi-Phase Vertical Take-Off and Landing Trajectory Optimization with Feasible Initial Guesses," *Aerospace*, Vol. 11, No. 1, 2023, p. 39. https://doi.org/10.3390/aerospace11010039.

[8] May, M. S., Milz, D., and Looye, G., "Dynamic Modeling and Analysis of Tilt-Wing Electric Vertical Take-Off and Landing Vehicles," *AIAA SCITECH 2022 Forum*, American Institute of Aeronautics and Astronautics, 2022. https://doi.org/10.2514/6.2022-0263.

[9] Li, B., Sun, J., Zhou, W., Wen, C.-Y., Low, K. H., and Chen, C.-K., "Transition Optimization for a VTOL Tail-Sitter UAV," *IEEE/ASME Transactions on Mechatronics*, Vol. 25, No. 5, 2020, pp. 2534–2545. https://doi.org/10.1109/tmech.2020.2983255.

[10] Kubo, D., and Suzuki, S., "Tail-Sitter Vertical Takeoff and Landing Unmanned Aerial Vehicle: Transitional Flight Analysis," *Journal of Aircraft*, Vol. 45, No. 1, 2008, pp. 292–297. https://doi.org/10.2514/1.30122.

[11] Oosedo, A., Abiko, S., Konno, A., and Uchiyama, M., "Optimal Transition from Hovering to Level-Flight of a Quadrotor Tail-Sitter UAV," *Autonomous Robots*, Vol. 41, No. 5, 2016, pp. 1143–1159. https://doi.org/10.1007/s10514-016-9599-4.

[12] Fredericks, W. J., McSwain, R. G., Beaton, B. F., and Klassman, D. F., "Greased Lightning (GL-10) Flight Testing Campaign," , 2017.

[13] Wang, M., Diepolder, J., Zhang, S., Söpper, M., and Holzapfel, F., "Trajectory optimization-based maneuverability assessment of eVTOL aircraft," *Aerospace Science and Technology*, Vol. 117, 2021, p. 106903. https://doi.org/10.1016/j.ast.2021.106903.

[14] Lu, Z., Hong, H., Diepolder, J., and Holzapfel, F., "Maneuverability Set Estimation and Trajectory Feasibility Evaluation for eVTOL Aircraft," *Journal of Guidance, Control, and Dynamics*, Vol. 46, No. 6, 2023, pp. 1184–1196. https://doi.org/10.2514/1.g007109.

[15] Vascik, P. D., "Systems Analysis of Urban Air Mobility Operational Scaling," Ph.D. thesis, Massachusetts Institute of Technology, Massachusetts, 2020.

[16] Al Haddad, C., Chaniotakis, E., Straubinger, A., Plötner, K., and Antoniou, C., "Factors affecting the adoption and use of urban air mobility," *Transportation Research Part A: Policy and Practice*, Vol. 132, 2020, pp. 696–712. https://doi.org/10.1016/j.tra.2019.12.020.

[17] Babetto, L., König, R., Fassnacht, J., and Stumpf, E., "Study On Public Acceptance of eVTOL: Safety & Noise," 2024. https://doi.org/10.25967/610319.

[18] Bauranov, A., and Rakas, J., "Urban Air Mobility and Manned eVTOLs: Safety Implications," *2019 IEEE/AIAA 38th Digital Avionics Systems Conference (DASC)*, 2019, pp. 1–8. URL https://api.semanticscholar.org/CorpusID:218472940.

[19] Thompson, E. L., Taye, A. G., Guo, W., Wei, P., Quinones, M., Ahmed, I., Biswas, G., Quattrociocchi, J., Carr, S., Topcu, U., Jones, J. C., and Brittain, M. W., "A Survey of eVTOL Aircraft and AAM Operation Hazards," *AIAA AVIATION 2022 Forum*, American Institute of Aeronautics and Astronautics, 2022. https://doi.org/10.2514/6.2022-3539.

[20] Basset, P.-M., Vu, B., Beaumier, P., Reboul, G., and Ortun, B., "Models and Methods at ONERA for the Presizing of eVTOL Hybrid Aircraft Including Analysis of Failure Scenarios," *Proceedings of the Vertical Flight Society 74th Annual Forum*, The Vertical Flight Society, 2018, pp. 1–15. https://doi.org/10.4050/f-0074-2018-12673.

[21] EASA, "Special Condition for Small-Category VTOL Aircraft," , 2019.

[22] May, M. S., Milz, D., and Looye, G., "Semi-Empirical Aerodynamic Modeling Approach for Tandem Tilt-Wing eVTOL Control Design Applications," *AIAA SCITECH 2023 Forum*, American Institute of Aeronautics and Astronautics, 2023. https://doi.org/10.2514/6.2023-1529.

[23] Phillips, W. F., *Mechanics of Flight*, John Wiley & Sons, Inc., 2004.

[24] Olson, E. D., "Semi-Empirical Prediction of Aircraft Low-Speed Aerodynamic Characteristics," *53rd AIAA Aerospace Sciences Meeting*, American Institute of Aeronautics and Astronautics, 2015. https://doi.org/10.2514/6.2015-1679.

[25] Kirkpatrick, D. G., and Murphy, R. D., "Planning Wind-Tunnel Test Programs for V/STOL Conversion Studies," *AIAA 3rd Aerodynamic Testing Conference*, 1968.

[26] Cook, J. W., "Exploration of Dynamic Transitions of Tiltwing Aircraft using Differential Geometry," Ph.D. thesis, University of Colorado, 2022.

[27] May, M. S., Milz, D., and Looye, G., "Towards the Determination of the Dynamic Transition Corridor for Tandem Tilt-Wing Aircraft," *AIAA AVIATION FORUM AND ASCEND 2024*, American Institute of Aeronautics and Astronautics, 2024. https://doi.org/10.2514/6.2024-4417.

[28] Chauhan, S. S., and Martins, J. R. R. A., "RANS-Based Aerodynamic Shape Optimization of a Wing Considering Propeller-Wing Interaction," *Journal of Aircraft*, Vol. 58, No. 3, 2021. https://doi.org/10.2514/1.C035991.

[29] Goldstein, S., "On the Vortex Theory of Screw Propellers," *This Issue*, Vol. 123, 1929. https://doi.org/10.1098/rspa.1929.0078.

[30] Veldhuis, L. L., "Propeller Wing Aerodynamic Interference," Dissertation, Delft University of Technology, Delft, Netherlands, 2005.

[31] Vatistas, G. H., Kozel, V., and Mih, W. C., "A Simpler Model for Concentrated Vortices," *Experiments in Fluids*, Vol. 11, No. 1, 1991, pp. 73–76. https://doi.org/10.1007/bf00198434.

[32] Torenbeek, E., *Synthesis of Subsonic Airplane Design*, repr. ed., Kluwer Academic Publ., Dordrecht [u.a.], 1999.

[33] Hoerner, S. F., *Fluid Dynamic Drag*, Hoerner Fluid Dynamics, 1965.